NIST Author Manuscript

NIST Author Manuscript

NIST Author Manuscript

Structural Properties of Kerogens with Different Maturities

Wei-Shan Chiang[||,†,‡], **Jin-Hong Chen**[||], **David Jacobi**[||], **Taner Yildirim**[†], **Danyal Turkoglu**[†], **Stacey Althaus**[||], **Yun Liu**[†,‡]

[||]Aramco Services Company: Aramco Research Center-Houston, Texas, USA

[†]Center for Neutron Research, National Institute of Standards and Technology, Gaithersburg, Maryland, USA

[‡]Department of Chemical and Biomolecular Engineering, University of Delaware, Newark, Delaware, USA

Abstract

The thermogenic transformation of kerogen into hydrocarbons accompanies the development of a pore network within the kerogen that serves as gas storage locations both in pore space and surface area for adsorbed gas within the source rock. Therefore, the successful recovery of gas from these rocks depends on the accessible surface area, surface properties, and interconnectivity of the pore system. These parameters can be difficult to determine because of the nanoscale of the structures within the rock. This study seeks to investigate the pore structure, surface heterogeneity, and composition of recovered kerogens isolated from source rocks with progressively increasing thermogenic maturities. Prompt gamma-ray activation analysis (PGAA), nitrogen and methane volumetric gas sorption, and small-angle neutron scattering (SANS) are combined to explore the relationship between the chemical composition, pore structure, surface roughness, surface heterogeneity, and maturity. PGAA results indicate that higher mature kerogens have lower hydrogen/carbon ratio. Nitrogen gas adsorption indicates that the pore volume and accessible specific surface area are higher for more mature kerogens. The methane isosteric heat at different methane uptake in the kerogens is determined by methane isotherms and shows that approximately two types of binding sites are present in low mature kerogens while the binding sites are relatively homogeneous in the most mature kerogen. The hysteresis effect of the structure during the adsorption and desorption process at different CD_4 gas pressures are studied. An extended generalized Porod's scattering law method (GPSLM) is further developed here to analyze kerogens with fractal surfaces. This extended GPSLM quantifies the surface heterogeneity of the kerogens with a fractal surface and shows that kerogen with high maturity is chemically more homogeneous, consistent with the results from methane isosteric heat. SANS analysis also suggests a pronounced surface roughness in the more mature kerogens. A microporous region circling around the nanopores, which contributes to high surface roughness and methane storage, is shown to develop with maturity.

Corresponding Authors: yunliu@nist.gov, jinhong.chen@aramcoservices.com.

Introduction

The U.S. Energy Information Administration (EIA) estimates that in 2016 there was about 447 billion cubic metre (Bcm) of dry natural gas produced directly from shale and tight oil resources in the United States. This was about 60% of total U.S. dry natural gas production in the year. Due to the success of extracting hydrocarbons from unconventional shale reservoirs, research on the pore structure of organic-rich source rocks has significantly increased.[1–5] However, there are still many fundamental questions related to the storage and transport of gas in shales. In addition to hydraulic fracturing stimulation, the production of gas from shales is ultimately controlled by two main factors: the gas in place (GIP) and the flow rate from the matrix into the fractures and then to the wellbore. Both of these factors are dependent on the maturity and the total organic carbon (TOC) of the shales. Successful recovery of gas from the matrix, however, is highly dependent upon the pore architecture and its connectivity in the source rocks. Understanding and quantifying the control exerted by these factors on production are the keys to increasing future shale gas production.

Organic-rich shales represent source rocks that consist of different organofacies, which are classified according to the organic matter type and mineral matrix.[6] Kerogen, the major component of organic matter, is an insoluble macromolecular organic polymer composed of three groups of macerals.[7] These macerals are the source for the hydrocarbons generated within the source rock as it is progressively buried and thermogenically transformed with time.[8] With burial and increasing temperature, the kerogen matures and begins to produce bitumen, then oil and gas, the abundance of which changes at different thermogenic stages.[9–11] This progressive hydrocarbon generation leads to a loss in volume of organic matter, which causes development of a pore network within the kerogen. As a result, intra-kerogen porosity provides a surface area and pore volume for the storage of hydrocarbons, in particular gas. Hydrocarbons, however, have been shown to be stored in a dual pore system within the source rock.[12] This system consists of a complex pore network within both the organic and inorganic matrices of the source rock that forms with burial, with pores ranging in size on average from 1 nm to 100 nm.[13, 14] Thus, the pore structure in shales is affected by many factors. It evolves with increasing maturity of the organic matter, and is influenced by differential compaction of different grain sizes during burial, all of which is determined by the changing mineralogy and amount and type of organic matter within the rock.[14–16]

Different types of techniques have been used for characterization of the pore structure and connectivity of shales from different reservoirs. These include helium porosimetry,[2, 5] low pressure gas adsorption of nitrogen (N_2)[1, 4, 5, 17, 18] and carbon dioxide (CO_2),[1, 5, 17, 18] mercury intrusion porosimetry (MIP),[1, 4] focused ion beam-scanning electron microscope (FIB-SEM),[19] helium ion microscopy (HIM),[2] and small-angle and ultra-small-angle neutron scattering (SANS/USANS),[1–4] and etc. These techniques discover the structure in different length-scale ranging from sub-nanometer to tens of micrometers and therefore can be used to obtain comprehensive information of micropore (< 2 nm), mesopores (2–50 nm), and macropore (> 50 nm).[3] Moreover, adsorption isotherms of light hydrocarbons[5, 17, 18, 20], especially methane, on shale rocks were determined to investigate the storage capacity of shale gas in the shales. However, since both the mineral and organic matter contribute to the total porosity in shales and the two components have very different structure and

mechanical properties, it is better to isolate the most important organic matter, i.e. kerogen, and investigate different factors that affect its structure and storage capacity.

In present study, we focus on determining the properties of the kerogen pore network at the nanoscale. The goal is to investigate the pore structure of kerogen, measure the compositional factors controlling its evolution, and understand its capacity to store natural gas, especially methane. To accomplish this goal we investigate kerogens with different maturities isolated from organic-rich shale rocks. The elemental contents, especially the hydrogen-to-carbon ratio, of the kerogens are determined by prompt gamma-ray activation analysis (PGAA). Pore structure and connectivity are studied by volumetric gas sorption isotherm measurements and small-angle neutron scattering (SANS).

Experimental Methods and Theories

Materials

Kerogens of different maturities were isolated from the source rock by using hydrofluoric acid (HF)-hydrochloric acid (HCl) digestion.[21] The chemical composition of the kerogen samples was measured by Weatherford using an elemental analyzer. Details of the sample preparation can be found in a previous paper by some of the authors.[22] The maturity of kerogen was characterized according to hydrogen/carbon ratios and %Ro equivalent calculated from T-max obtained from pyrolysis.

Small-angle neutron scattering (SANS)

Small-angle neutron scattering (SANS) measurements were performed at nSoft-10m SANS and NGB-30m SANS at the National Institute of Standards and Technology (NIST) Center of Neutron Research (NCNR). Note that NGB-30m SANS is one of instruments in the Center for High Resolution Neutron Scattering (CHRNS) at NCNR. The wavelength of incident cold neutrons, λ, was chosen to be 5 Å or 6 Å and the sample-to-detector distances (SDD) were selected to cover a scattering vector (Q) range from 0.0014 to 0.568 Å^{-1}. SANS data were corrected for sample transmission, background scattering, and detector sensitivity to obtain an absolute intensity. This correction method is based on a standard procedure described in a previous publication.[23]

The kerogen samples were degassed under vacuum for 48 hours. The samples were then transferred to sample cells in a helium gas filled glovebox. SANS measurements were performed on dry samples contained in Titanium cells with quartz windows. The measurement was conducted up to $Q = 0.568$ Å^{-1}. High pressure (HP) cells made of stainless steel with sapphire windows, were used to contain kerogen samples subjected to gas loading at high pressures. The use of the HP cells limited the Q range of the SANS data only up to $Q = 0.3$ Å^{-1}. The pressure of the loading gas, deuterated methane (CD_4), was controlled by 100HLf hazardous location syringe pump purchased from Teledyne Isco. The SANS measurement was first conducted on the kerogens under vacuum using a turbo pump linked to the syringe pump. Helium gas at 31.1 MPa was then loaded into the kerogens for *in-situ* SANS measurement. After the measurement, the helium gas was evacuated with the turbo pump. CD_4 with different pressures was loaded into the samples for the *in-situ* gas loading

SANS study. All the measurements were maintained at 21 °C by the circulating cooling bath system using a mixture of 50 % ethylene glycol and 50 % water. CD_4 was purchased from Cambridge Isotope Laboratories, Inc. Thermodynamic properties of the bulk methane were calculated using NIST standard reference database software REFPROP.[24]

Volumetric gas adsorption isotherm

Gas sorption isotherm measurements were performed on a carefully calibrated and high accuracy Sieverts apparatus under computer control. Instrument and measurement-protocol details have been published elsewhere.[25] Helium and hydrogenated methane (CH_4) gases were of Research or Scientific grade, with a minimum purity of 99.999 %.

Prompt gamma-ray activation analysis (PGAA)

Cold neutron prompt gamma-ray activation analysis (PGAA) was performed at the NGD beamline at NCNR. The details of the facilities and methodology can be found elsewhere.[26] The samples were vacuumed for two days prior to the measurement to remove residual moisture.

Generalized Porod's Scattering Law Method (GPSLM)

In many porous materials, the equation for the Porod's scattering law region can be described by the generalized Porod's scattering law[22]:

$$I(Q) \xrightarrow{Q \to \infty} 2\pi \left\langle \Delta \rho^2 \right\rangle_s Q^{-4} \frac{S_T}{V} = C_P Q^{-4}$$

(1)

Where $\left\langle \Delta \rho^2 \right\rangle_s \equiv \frac{1}{S_T} \int (\rho(S) - \rho_f)^2 \, dS$ and The GPSLM has been developed previously to study the surface heterogeneity of porous materials by studying the contrast variation in the Porod's scattering law region. Here we briefly describe the GPSLM and the details can be found in the previous paper.[22] $IR(Q, \rho_f)$ is defined as the ratio between the intensity of sample loaded with fluid with SLD $= \rho_f$ to the intensity of dry sample ($\rho_f = 0$) at the same Q, i.e. $IR(Q, \rho_f) \equiv \frac{I(Q, \rho_f)}{I(Q, \rho_f = 0)}$. At Porod's scattering region, $IR(Q, \rho_f)$ is independent of the Q value, i.e. $IR(Q, \rho_f) = IR(\rho_f)$. In current case, the fluid loaded into the kerogen samples is CD_4 and therefore $\rho_f = \rho_{CD4}$. According to GPSLM, $IR(\rho_f)$ is a parabolic function of ρ_f in the Porod's scattering Q range described in eq 1[22]:

$$IR(\rho_f) = \frac{(\rho_f - \rho_A)^2}{\rho_{2M}^2} + \Delta_H^2$$

(2)

eq 2 has the minimum $IR_{min}(\rho_{f,min})$ at $\rho_{f,min}$, where

$$\rho_{f,min} = \rho_A$$

$$(3)$$

$$IR_{min}(\rho_{f,min}) = \Delta_H{}^2$$

$$(4)$$

For the simple situation where all the pores in the heterogeneous sample are accessible to guest fluid and the SLD of solid matrix is not changed with the guest fluid, the parameters in eqs 2–4, i.e. ρ_A, $\rho_{2M}{}^2$, and $\Delta_H{}^2$, can be formulated as follow:

$$\rho_A \equiv \frac{1}{S_T} \int \rho(S)\, dS$$

$$(5)$$

$$\rho_{2M}{}^2 \equiv \frac{1}{S_T} \int \rho(S)^2\, dS$$

$$(6)$$

$$\Delta_H{}^2 \equiv \frac{\rho_M{}^2 - \rho_A{}^2}{\rho_{2M}{}^2} = \frac{\left[\frac{1}{S_T}\int (\rho(S) - \rho_A)^2 dS\right]}{\rho_{2M}{}^2}$$

$$(7)$$

$$\frac{S_T}{V} = \frac{Q^4 I(Q, \rho_f = 0)}{2\pi} \frac{1}{\rho_{2M}{}^2} = \frac{C_P(\rho_f = 0)}{2\pi} \frac{1}{\rho_{2M}{}^2}$$

$$(8)$$

$\rho(S)$ is the SLD of the solid matrix at the interface S and the variation of $\rho(S)$ with S gives the surface heterogeneity of the material. From eqs 5–7, ρ_A, $\rho_{2M}{}^2$, and $\Delta_H{}^2$ are simply the surface averaged SLD, the surface averaged second moment of SLD, and the normalized surface heterogeneity of the sample. S_T and V are the total surface area and the total volume of the sample seen by the neutron beam. $C_P(\rho_f = 0)$ is the Porod's scattering constant at the guest fluid SLD $\rho_f = 0$. According to eqs 3 and 4, by plotting the experimental values of $IR(\rho_f)$ as a function of ρ_f and finding the minimum position of the parabolic function, we can directly determine the values of ρ_A and $\Delta_H{}^2$ of the samples. $\rho_{2M}{}^2$ is calculated through

$\rho_{2M}{}^2 = \frac{\rho_A{}^2}{1 - \Delta_H{}^2}$ (eq 7), and can be further used to determine the total surface area S_T (eq 8).

Results and Discussions

Element Analysis of Kerogens

The sensitivity of neutrons to hydrogen atoms allows for the accurate determination of atomic ratios of hydrogen relative to some of the other elements composing the kerogens. The elemental atomic ratios of our kerogens are obtained using PGAA. The results are listed in Table 1. It is observed that the relatively high H/C ratio of the investigated samples becomes lower with the increasing R_0. This trend represents increasing maturity as hydrogen is progressively lost relative to carbon as kerogen generates hydrocarbons. Thomas *at al.*[27] also found the same trend of decrease in H/C ratio with the increased maturity of kerogen. Table 1 also shows nitrogen content decreases slightly with the maturity as well. Wang *et al.*[28] characterized the organic nitrogen in the oil shale kerogens, and no clear trend was found between total nitrogen content with H/C ratio. On the other hand, Zhao found two kerogens from different locations with similar R_0 (~ 0.99 % and 1.06 %) have similar nitrogen content (1.70 wt% and 1.82 wt%). Table 1 also indicates there are iron-containing mineral phases present, especially for Sample 2. Our own X-ray diffraction patterns have also identified both pyrite and marcasite (FeS_2) in the kerogen. These phases typically are insoluble during the HF-HCl digestion and are left behind after removal of the more soluble mineral matter.[27] Table 2 shows that two times of Fe/C ratio is very close to or even larger than the S/C ratio, suggesting that very little organic sulfur is present in the kerogens.

Volumetric Isotherm Measurements for Nitrogen and Methane Adsorption in Kerogens

To determine the surface area for each kerogen, gas adsorption was conducted on each sample using nitrogen (N_2) and methane (CH_4). Figure 1 shows the volumetric isotherm measurements for nitrogen (N_2) adsorption at 77 K for all four kerogens. Except for Sample 4, the isotherm curves indicate very small amounts of N_2 adsorption before N_2 condensation occurred in the macropores. The N_2 isotherm curve of Sample 4 can be classified as the type II isotherm according to the IUPAC Classification Scheme[29] as indicating by micropore filling at $P/P_0 < 0.2$, the curve increases gradually at $P/P_0 > 0.2$ and eventually increases upward when $P/P_0 \approx 1$. The BET surface area, S_{BET}, obtained from N_2 adsorption at 77 K for the four kerogens are listed in Table 2. S_{BET} shows the following trend: Sample 4 > Sample 3 > Sample 2 > Sample 1. Therefore, the more mature kerogen, as indicated by the higher vitrinite reflectance (R_0), exhibits an increase in specific surface area. The total pore volume is also listed in Table 2. It is calculated from the volume of N_2 condensing in the pores at 77 K and $P/P_0 \approx 0.98$ by assuming bulk density for N_2. Sample 4 with largest maturity in these 4 samples shows the largest amount of pore volume too. Rexer *et al.*[5] studied the Posidonia shales and their isolated kerogens using gas adsorption. They found similar magnitude of BET surface area (7.5 m^2/g to 68.1 m^2/g) and pore volume (0.07 cc/g to 0.11 cc/g) in the kerogens with R_0 between 0.53% and 1.45% compared with the kerogens in this study (BET surface area from 5.9 m^2/g to 78.0 m^2/g and pore volume from 0.06 cc/g to 0.16 cc/g for R_0 between 0.62 % to 2.26 %). The trends of BET surface area and pore volume changing with maturity found by Rexer *et al.*[5] are also similar to what we found here.

The isosteric heat, Q_{st}, for the four kerogens is plotted in Figure 2 as a function of methane adsorption uptake. Details of the method can be found elsewhere.[27] The isosteric heat at zero adsorption limit, $Q_{st,0}$, for the kerogens is listed in Table 2. $Q_{st,0}$ is larger for the less mature samples (Sample 1, Sample 2, and Sample 3) than the most mature (Sample 4). Figure 2 shows the Q_{st} curves behave very differently for the three kerogens with less maturity and the most mature Sample 4. For Sample 1, Sample 2, and Sample 3, there are approximately two types of binding sites: (1) the very strong binding sites with $Q_{st} > 24$ kJ/mol and with very small population as shown in low methane uptake; (2) weak binding sites with $Q_{st} < 24$ kJ/mol at relatively large methane adsorption. On the other hand, for Sample 4, there are no sign of strong binding sites and only weak binding sites are present. The Q_{st} curves show that the binding sites on the surfaces of Sample 4 are more homogeneous than other kerogens. The SANS analysis that will be discussed below also shows that the most mature kerogen has the lowest surface heterogeneity. This further supports the claim of the homogeneity difference exists between the low-maturity and high-maturity samples.

SANS Results for Dry Kerogens

Figure 3 shows the absolute SANS intensity $I(Q)$ subtracted by a constant incoherent background and normalized by the kerogen mass inside the neutron beam for the four dry kerogens, i.e. kerogens without loading gas. The SANS patterns follow a decaying, power-law trend over a low Q region for all the four samples. Except for the most mature sample, Sample 4, the low Q region can be described by the generalized Porod's scattering law[22], $I(Q) \xrightarrow{Q \to \infty} 2\pi \left\langle \Delta \rho^2 \right\rangle_s Q^{-4} \frac{S_T}{V} = C_P Q^{-4}$, where $\left\langle \Delta \rho^2 \right\rangle_s \equiv \frac{1}{S_T} \int (\rho(S) - \rho_f)^2 \, dS$ is the mean square deviation of scattering length density (SLD), $\rho(S)$, integrating through all interface S in the sample, whose total interfacial area is S_T. ρ_f is the SLD of the gas molecules filling the pores. In the special case of dry sample, $\rho_f = 0$. V is the total volume of the sample seen by the neutron beam. $C_P = 2\pi \left\langle \Delta \rho^2 \right\rangle_s \frac{S_T}{V}$ is the Porod's scattering constant and can be easily determined by fitting the scattering intensity curve $I(Q)$ with $I(Q) = C_P Q^{-4}$. The Porod's scattering ($I(Q) \propto Q^{-4}$) observed in the less mature samples (Sample 1, Sample 2, and Sample 3) covers the Q up to about $Q_{PS} \approx 0.03$ Å^{-1} , which is the largest Q value following the Porod's scattering described in eq 1. In contrast, Q_{PS} for Sample 4 is much smaller than 0.03 Å^{-1} indicating that Sample 4 has more fine structures (nanopores) at the length scale around 20 nm or larger compared with Sample 1, 2 and 3.

According to the literature, the incoherent background is usually determined by the slope of the Porod plot based on $I(Q) * Q^4 v_s Q^4$.[2, 27, 30] Here we adopted the same method by using the data $Q > 0.45$ Å^{-1} to find the background. However, Figure 3 shows that even after subtracting a constant background, there are still features at high Q region ($Q > 0.1$ Å^{-1}), indicating that there is heterogeneity in the small length scale $\approx \frac{2\pi}{Q_{bump}} \approx 3$ nm in the kerogen solid matrices, where $Q_{bump} \approx 0.2$ Å^{-1} is the bump location at high Q SANS patterns. Previous studies also showed the structure heterogeneity in small length scale, most likely due to small mesopores or micropores, suggested by the high Q SANS data.[2, 3] Although Porod plot is used to find the background, there may be residual coherent contribution in the

background found in this way, i.e. the incoherent background may be over-subtracted and the coherent scattering features seen in high Q can be larger than what we expect. Therefore, any analysis in the high Q region should be carried out with caution.

SANS Results for Methane Adsorption in Kerogens

Psarras *et al.*[17] simulated kerogen surface with different surface functionalities and by using molecular simulation they showed that the pore chemistry of kerogens can greatly influence the storage capacities of methane. Therefore, understanding the surface properties, especially the surface heterogeneity, of kerogens is important. We investigate the nanoscale structures of isolated kerogens here using deuterated methane, CD_4, as the probing gas combined with SANS technique.

The gas adsorption of methane in Sample 1, 2, and 3 have been studied previously by us using SANS to extract the average scattering length density and the surface heterogeneity using the Generalized Porod's Scattering Law method (GPSLM). Here, we study the reversibility of gas loadings in Sample 1, 2 and 3, at different pressures during both the adsorption and desorption processes that have not be discussed before. In addition, we investigate Sample 4 with even higher maturity and compare the result with Sample 1, 2, and 3.

Similar to the previous studies on Sample 1, 2 and 3, the structure stability of Sample 4 is first tested with helium gas. Figure 4(a) shows the SANS data for Sample 4 before and after loading 31.1 MPa helium gas. For the completeness, we have also shown the results for Sample 1, 2 and 3 in the same figure. Because helium has very low neutron scattering length density (SLD) even at 31.1 MPa (SLD $\approx 2.3 *10^{-7}$ Å^{-2}), it "looks like" vacuum for neutrons. The almost identical SANS curves for dry kerogens and helium-loading kerogens shown in Figure 4(a) indicate that kerogen structure is not changed by inert gas at the pressure range being studied.

Figure 4(b),(c),(d),(e) show the SANS intensity data for Sample 1, Sample 2, Sample 3, and Sample 4, respectively, loaded with CD_4 at pressure ranging from 0 MPa to 31.1 MPa for both methane desorption (solid squares) and adsorption (empty circles) process. In our SANS experiment procedure, we measured the dry kerogens first, loaded CD_4 directly up to 31.1 MPa, and conducted desorption measurement. Then we vacuumed the kerogens using turbo bump for 30 min. Then, the adsorption experiment was conducted.

By comparing the data of both the adsorption and desorption process, the structure of all kerogen samples are fully reversible. The SANS curve before loading gas (the "0 MPa" curve in Figure 4) and SANS curve after loading gas and vacuuming the system (the "0 MPa (Evacuate)" curve in Figure 4) for each dry kerogen are identical for all the four samples, confirming that the kerogen structure is the same with the original state after loading high pressure CD_4 and vacuuming the gas.

Previous studies[18, 31] claimed, though indirectly, kerogens are likely swollen by hydrocarbons. Zhao *et al.*[18] found sorption hysteresis of the light hydrocarbons, including methane even though with much less intense hysteresis, in shale and kerogen. They

suggested that the hysteresis may be due to the reversible structure changes of organic matter caused by hydrocarbons. The sorption measurements carried by Zhao *et al.*[18] was at low pressure region up to 3.5 MPa while our SANS measurements cover wider and higher pressure region to 31.1 MPa. Compared with isotherm gas adsorption, SANS is a relatively direct method to detect the structural properties of materials such as pore structure and methane density. Our SANS measurements for CD_4 desorption and adsorption give almost identical curves for low maturity Sample 1 (Figure 4(b)) and Sample 2 (Figure 4(c)) in the pressure range up to 31.1 MPa. For high maturity Sample 3 (Figure 4(d)) and Sample 4 (Figure 4(e)), the SANS curves measured are also identical at pressure below 20 MPa for both the adsorption and desorption process, but show a slight difference at the pressure above 20 MPa. Figure 4 suggests it is possible that at high pressure (above 20 MPa) for Sample 3 and 4, the structure of solid kerogen matrix of the high maturity samples may be more sensitive to the hydrocarbon interaction at high pressure. But as mentioned before, the structure observed by SANS is identical before and after the gas loading when all gas molecules are pumped out. Therefore, this structure hysteresis at high pressure is due to a reversible structure change.

Surface Heterogeneity Analysis from Generalized Porod's Scattering Region at Low Q ($Q < 0.03$ Å^{-1})

Because the SANS data of dry kerogens and kerogens loaded with 31.1 MPa helium (Figure 4(a)) are very similar, we assume the structure change of solid kerogen matrix due to CD_4 loading up to 31.1 MPa is negligible. The intensities of all the samples loaded with CD_4 follow the power-law Q dependence in the low Q region similar to the corresponding dry samples (Figure 4(b)-(e)).

As previously reported already, the SANS data at low-Q region after loading CD_4 follow Porod's scattering ($I(Q) \propto Q^{-4}$) in Sample 1, 2, and 3, the generalized Porod's scattering law method (GPSLM)[22] that was developed in our previous work can be applied to our samples. The average SLD, the surface heterogeneity, and the total surface area can be determined accurately using the GPSLM even for the materials with large heterogeneous surfaces. Note that GPSLM is a non-destructive method that can be used to extract the surface heterogeneity of the "bulk" heterogeneous sample. Moreover, it is model-independent and does not require any assumption of the shapes of the pores or particles.

However, Sample 4 does not follow Porod's scattering described in eq 1 because it has the scattering pattern of $I(Q) \sim Q^{-3.3}$ instead of $I(Q) \propto Q^{-4}$. This surface fractal dependence is commonly observed in many porous materials. In order to apply the GPSLM to obtain the surface heterogeneity information, the extended GPSLM method is developed here to investigate the surface variation for fractal surfaces.

For a system with a fractal surface with the fractal dimension, D_f, the scattering intensity, $I(Q)$ is proportional to $\dfrac{1}{Q^{6-D_f}}$.[32, 33] D_f has a value between 2 and 3. Thus, sample 4 has a

surface fractal of 2.7 indicating that its surfaces are not smooth. In contrast, Sample 1, 2 and 3 has $\frac{1}{Q^4}$ dependence at similar Q range with the smooth surfaces (D_f=2).

For scattering from a fractal surface, the intensity can be expressed as[33]

$$I(Q) = (\Delta \rho)^2 \frac{S}{V} l^{D_f - 2} \frac{\pi \Gamma\left(5 - D_f\right) \sin\left(\frac{\pi(3 - D_f)}{2}\right)}{3 - D_f} \frac{1}{Q^{6 - D_f}}$$

(9)

where S is the smooth surface area measured by a probe particle with the length scale proportional to l. If we define $S_a = S l^{D_f - 2} \frac{\Gamma\left(5 - D_f\right) \sin\left(\frac{\pi(3 - D_f)}{2}\right)}{2(3 - D_f)}$, the above equation can then be expressed as

$$I(Q) = 2\pi (\Delta \rho)^2 \frac{S_a}{V} \frac{1}{Q^{6 - D_f}}$$

(10)

For D_f=2, $S_a = S$. Equation (10) is reduced to the classic Porod's law scattering. If the surfaces have similar surface fractal, but with different contrasts, Equation (10) can be written in a more general form as

$$I(Q) = 2\pi \left\langle \Delta \rho^2 \right\rangle_s \frac{S_a}{V} \frac{1}{Q^{6 - D_f}}$$

(11)

where $\left\langle \Delta \rho^2 \right\rangle_s \equiv \frac{1}{S_a} \int (\rho(S) - \rho_f)^2 \, dS$. This is almost identical to the general term of the Porod's law scattering, $I(Q) \xrightarrow{Q \to \infty} 2\pi \left\langle \Delta \rho^2 \right\rangle_s \frac{S_T}{V} \frac{1}{Q^4}$, except the different power law dependence on Q.[22]

If the fluid loaded in pores does not alter the fractal structure, the change of the scattering intensity for Equation (11) is only due to the change of the contrast term $\left\langle \Delta \rho^2 \right\rangle_s$. Thus the derivation of the GPSLM for the smooth surface can be applied here, and results in

$$\rho_A \equiv \frac{1}{S} \int \rho(S) \, dS$$

(12)

$$\rho_{2M}{}^2 \equiv \frac{1}{S} \int \rho(S)^2 \, dS$$

(13)

$$\Delta_H{}^2 \equiv \frac{\rho_M{}^2 - \rho_A{}^2}{\rho_{2M}{}^2} = \frac{\left[\frac{1}{S_a}\int(\rho(S) - \rho_A)^2 dS\right]}{\rho_{2M}{}^2}$$

(14)

$$\frac{S_a}{V} = \frac{Q^{6 - D_f} I(Q, \rho_f = 0)}{2\pi} \frac{1}{\rho_{2M}{}^2} = \frac{C_P(\rho_f = 0)}{2\pi} \frac{1}{\rho_{2M}{}^2}$$

(15)

$\rho(S)$ is the SLD of the solid matrix at the fractal interface S and the variation of $\rho(S)$ with S gives the surface heterogeneity of the material.

The results of Equation (12)-(15) are almost identical to the results of the GPSLM. ρ_A and $\rho_{2M}{}^2$ are averaged values through all fractal surfaces. The surface heterogeneity is also due to the variation of the SLD along different fractal surfaces. Note the obtained S_a from Equation (15) is not a surface area except for $D_f = 2$.

Sample 4 is thus analyzed using this extended GPSLM method. We fit the low-Q slope to obtain the coefficient and calculate the ratio of the low-Q slope. The results of ρ_A, $\rho_M{}^2$, and Δ_H obtained from the extended GPSLM are shown in Table 3. In order to compare with the previous results, we also listed the values for Sample 1, 2, and 3. Even though S_a is proportional to the true surface area for a fractal surface, we need to be careful when interpreting the surface area obtained from the fractal surface. But the definition of ρ_A, $\rho_M{}^2$, and Δ_H is still the same with the previous GPSLM. Hence, the results of Sample 4 can be directly compared with those of Sample 1, 2 and 3.

Table 3 shows that ρ_A keep increasing with the further increase of the kerogen maturity, consistent with the previous observation. Thus, kerogens with high maturity have low hydrogen content and this is consistent with the low H/C ratio found in PGAA results (see Table 1) and other literatrue.[27] This is because hydrogen has negative scattering length. Samples with less H have larger SLD. The average SLD along the accessible surface is about $5.9 \times 10^{-6} \text{Å}^{-2}$ for Sample 4 indicating that there are very few hydrogen along the surface of the materials. (Note that the SLD for graphite is about $7.6 \times 10^{-6} \text{Å}^{-2}$.)

The decrease in Δ_H with maturity shown in Table 3 indicates that the kerogens become more homogeneous during maturation process. The surface heterogeneity for both Sample 3 and Sample 4 are almost zero based on our fitting results. Thus, the surface SLD of Sample 3 and 4 are very uniform. The smaller heterogeneity in more mature kerogen is also suggested in Q_{st} curves found in Figure 2, where the difference between Type A and Type B adsorption sites is smaller in Sample 4 than in Sample 1. For Sample 1, 2 and 3, the extracted surface

area is similar to the BET surface area. Future work will be needed to understand the difference between S_a and the true surface area from a fractal surface.

Debye Anderson Brumberger (DAB) Analysis for Middle Q Range (0.03 Å^{-1} < Q < 0.1 Å^{-1})

For this middle Q range, the scattering patterns may slowly deviate from the power law dependence. We carefully look into the subtle features in this Q range by removing the contributions from both low Q and high Q. Two scattering contributions are subtracted from the absolute intensity: (1) a constant background, bk,[2, 27, 30] found by the slope of the plot $I(Q) * Q^4 v_s. Q^4$ in the Q range between 0.1 Å^{-1} to 0.3 Å^{-1} and (2) the contribution of power-law scattering determined by fitting the low Q region with $I(Q) = C(P)Q^{-(6 - d_f)}$, where $C(P)$ is the pre-factor of the power law scattering that depends on the pressure and SLD of loaded CD$_4$. Note that the effect from its contribution in the Q range of 0.03 Å^{-1} < Q < 0.1 Å^{-1} by the low Q is small and does not affect the fitting results much.

Natural materials such as shales usually have complex structures due to many factors, such as the complexity of the size distribution of the particles and pores, the different shape of the particles and pores, the variation of the chemical compositions, etc. in the samples. It is thus difficult to obtain quantitative information from SANS data for these complex samples. Despite the difficulty, there were many attempts to use polydisperse spherical pore (PDSP) model.[34,3534, 35] In order to avoid introducing too many fitting parameters but focus on extracting the "average" characteristic length, Debye Anderson Brumberger (DAB) model[36, 37] is used here to obtain ξ for the middle Q range at different methane loading pressure. DAB is derived for scattering from a randomly distributed and two-phase system with pair correlation function formulated as $\gamma = \exp(-r/\xi)$. ξ is the correlation length. Therefore, in this analysis we approximate the system as "average" two phase system composed of "average" matrix with an average SLD (phase 1) and pores filled with fluid (phase 2) in the length scale of 6 nm < L < 20 nm (corresponding to the Q range of 0.03 Å^{-1} < Q < 0.1 Å^{-1}). Note that because the SLD of Sample 3 and 4, this approximation of two phase systems is very reasonable for Sample 3 and 4. Even though Sample 1 and 2 may have multiple phase, the obtained apparent correlation length will be still very useful. This correlation length, ξ, can be considered qualitatively related with the average pore size. Larger ξ implies larger pores in the sample.

After subtracting the two scattering contributions mentioned above, the remaining intensity is the coherent scattering and is fitted with DAB model using the Q range of 0.03 Å^{-1} < Q < 0.1 Å^{-1} for the four kerogens. At Q > 0.1 Å^{-1}, the data are highly influenced by the incoherent background and accurate quantitative analysis is difficult. According to DAB model:

$$I(Q) = I_0 \frac{1}{\left[1 + (Q\xi)^2\right]^2}$$

(16)

In eq 16, the forward scattering I_0 and ξ are the fitting parameters. The DAB fitting results for the four kerogens are plotted as a function of pressure in Figure 5(a) and 5(b) for I_0 and ξ, respectively. The scenario is quite different between less mature samples and the most mature sample.

For less mature samples (Sample 1 and Sample 2), I_0 slightly increases with the gas pressure and ξ almost maintains as a constant as ≈ 9 Å, similar to that of the dry kerogen (Pressure $P = 0$ MPa). This suggests that the interface between some very small pores and the matrix may not be accessible to the guest fluid CD_4. For example, there may be small number of solid pockets with very different SLD than the rest of the solid matrix and these pockets are imbedded in the matrix and cannot be accessed to CD_4 molecules. This is consistent with some previous works[2, 3] suggesting the existence of the inaccessible pores.

For the most mature sample (Sample 4), both I_0 and ξ significantly decrease with pressure. I_0 decreases continuously with pressure as expected for the accessible pores filled with CD_4. However, it is surprising that ξ does not maintain as constant, but decreases continuously with pressure for Sample 4. We propose that the mature Sample 4 has lots of pores with the average pore size at the length scale of the obtained correlation length (≈ 28 Å). And the wall of these pores has large surface roughness due to the large population of micropores on the pore surface. These micropores form corona regions around the pores. When increasing the CD_4 pressure, the corona regions of these pores are continuously filled by CD_4 with higher density than the bulk CD_4 density.[38, 39] Moreover, the SLD contrast between the CD_4 in the corona regions and solid kerogen decreases with pressure and the corona regions become less distinguishable with the solid kerogen to neutrons. The dominant SLD contrast after CD_4 filling is the rest of the pores filled with CD_4 with density similar to CD_4 bulk density and kerogen with corona regions filled with denser CD_4. This micropore filling process on the corona region of the pore wall is therefore equivalent to the decrease of the pore size. The importance of surface roughness on the methane adsorption was also discussed in previous studies for mesoporous materials.[38, 39] Surface roughness is found to strongly enhance methane adsorption in the model materials. It is expected that nature materials such as shale rocks can have much more surface roughness.

Sample 3 has combined trend that I_0 and ξ decrease first, increase again, and approach to a constant at higher pressure. The scenario combines both situations of most mature Sample 4 and least mature Sample 1 and Sample 2. There are notable amount of both accessible pores with rough surface and small number of non-accessible pockets and their effects are dominated in low and high pressure, respectively. Therefore, the change of I_0 and ξ for Sample 3 has combined trends between low- and high-maturity samples.

It should be noticed that the Q range used in DBA analysis detects the length scale much smaller than the GPSLM or the extended GPSLM analysis method ($Q < 0.03$ Å^{-1}). During these analysis, the assumption that all pores are accessible to the fluid is used and this assumption refers to the pores with size falling into the Q range with length scale > 20 nm. Even though there are some inaccessible tiny pores (< 20 nm) imbedded in the solid matrix especially in low-maturity samples, the neutrons "see" them as part of the matrix in the low

Q range. That is to say, the matrix SLD, $\rho(S)$, in eq 5–8 is the "average" SLD of the solid part, including the tiny solid pockets, and both the inaccessible and accessible "tiny" pores. The tiny pores and solid pockets seen in the Q range used by DBA analysis are all part of the matrix in the larger length scale. A more comprehensive theory is developed recently to discuss this situation.[40]

Structure Heterogeneity at Small Length Scale Suggested at SANS Data at High Q ($Q > 0.1$ Å^{-1})

Figure 6(a) shows the SANS intensity at $Q = 0.2$ Å^{-1}, $I\left(Q = 0.2 \,\text{Å}^{-1}\right)$, as a function CD$_4$ pressure for the four kerogens together with the constant incoherent background, bk. bk is determined by the slope of the plot $I(Q) * Q^4 v_s . Q^4$ by using the data between 0.1 Å^{-1} to 0.3 Å^{-1}. Q= 0.2 Å^{-1} is chosen because it is where the "bump" at the high Q SANS data is located after subtracting the incoherent background (see Figure 3), i.e. $Q_{bump} \approx 0.2$ Å^{-1}. This bump indicates that there is some structure in small length scale of $\frac{2\pi}{Q_{bump}}$. With increasing CD$_4$ pressure, both $I\left(Q = 0.2 \,\text{Å}^{-1}\right)$ and bk increase almost monotonically for all the four samples. The fact that $I\left(Q = 0.2 \,\text{Å}^{-1}\right)$ is much larger than bk confirms that the SANS intensity at high Q is contributed from both the incoherent scattering of combined solid kerogen and CD$_4$ and the coherent scattering from structure at the small length scale of the sample.

As mentioned above, data at $Q > 0.1$ Å^{-1} are very sensitive to bk. This can be seen from Figure 6 which plots the SANS intensity at $Q = 0.2$ Å^{-1} after subtracting bk, i.e. $I\left(Q = 0.2 \text{Å}^{-1}\right) - bk \equiv I_{coh}\left(Q = 0.2 \text{Å}^{-1}\right)$, where coh represents coherent scattering. The value for $I_{coh}\left(Q = 0.2 \text{Å}^{-1}\right)$ fluctuates significantly especially at low pressure. Therefore, we only provide a qualitative discussion instead of detailed quantitative analysis in this Q range.

If the bump shown in SANS data is due to accessible nanopores (see Figure 3), the decrease in coherent scattering with pressure is expected. This is because the SLD of CD$_4$ in the pores increases, and SLD of the solid matrix remains the same. Although Figure 6(b) shows some change in $I_{coh}\left(Q = 0.2 \text{Å}^{-1}\right)$ with CD$_4$ pressure, the change is only within a few error bars and maintains as a relatively constant level. With the data quality at this Q range, we can only suggest that there are some structures in the length scale $\frac{2\pi}{Q_{bump}} \approx 3$ nm that are inaccessible to CD$_4$ and lead to unchanged or slightly increasing intensity with pressure.

Conclusions

Prompt gamma-ray activation analysis (PGAA), volumetric gas adsorption isotherm for nitrogen and methane, and *in-situ* gas loading small-angle neutron scattering (SANS) are conducted on four kerogens with different maturities isolated from natural shale rocks. PGAA shows that the more mature sample has lower hydrogen/carbon ratio as expected

together with the change of other elements. The volumetric nitrogen isotherm curves show higher pore volume and specific surface area for more mature kerogens. The isosteric heat for methane adsorption indicates that there are approximately two types of adsorption sites in low maturity kerogens: one is strong binding site with higher isosteric heat but smaller population, and another is weak binding site with lower isosteric heat but larger population. For the most mature kerogen, the isosteric heat is more uniformly distributed and therefore the nature of the binding sites are more homogeneous.

The reversibility of several kerogen samples by the gas (CD_4) loading is investigated using SANS. For all studied kerogens, the structures measured by SANS are identical before and after the gas loading. The SANS patterns at different gas (CD_4) pressures are identical for less mature kerogens (Sample 1 and 2) for both the adsorption and desorption process indicating that there is no hysteresis effect. For samples with large maturity (Sample 3 and 4), SANS patterns are identical at relatively small pressures (less than 20MPa) for both the adsorption and desorption process. However, for the pressure larger than 20MPa, the SANS patterns show slight difference for the adsorption and desorption process. Therefore, it is possible that there may be some hysteresis effect for kerogens with high maturity (Sample 3 and 4). But this structural hysteresis is found to be due to a reversible structure change.

One of kerogen sample shows the feature of fractal surfaces in SANS patterns. A new theory is developed by extending the generalized Porod's scattering law method (GPSLM) to investigate the surface heterogeneity of materials with fractal surfaces. By applying the extended GPSLM method to analyze the most mature sample (Sample 4), the results indicate that the average SLD increases with maturity, consistent with the low hydrogen content found in PGAA, and the decrease of the surface compositional heterogeneity with the increased maturity of kerogens, consistent with the isosteric heat results. The Debye Anderson Brumberger (DAB) analysis is used to analyze the SANS pattern at the middle Q range (between 0.03 Å^{-1} and 0.1 Å^{-1}). There seems to have inaccessible interfaces in less mature samples. It also indicates that for the most mature kerogen (Sample 4), there seems to have very small pores on the wall of large pores suggesting a rough surface of large pores.

The implication of using SANS for probing the structure and connectivity of the pore systems reveals the chemical composition distribution on surface, a changing surface roughness, and the increased accessible pores with the increased maturity. It is speculated that the loss of hydrogen relative to carbon in kerogen with maturity, detected by both PGAA and SANS, eventually leads to the development of microporous, corona encircled regions which are accessible to the methane being generated. These microporous regions could be areas within kerogen where methane could be condensed based on the contrast in the SLD hinted from SANS results. This study illustrates the challenges towards estimating the hydrocarbons in place accurately for the determination of potential future productivity of shale gas prospects as source rock reservoirs.

Supplementary Material

Refer to Web version on PubMed Central for supplementary material.

Acknowledgements

Reference

1. Clarkson CR; Solano N; Bustin RM; Bustin AMM; Chalmers GRL; He L; Melnichenko YB; Radlinski AP; Blach TP, Pore structure characterization of North American shale gas reservoirs using USANS/SANS, gas adsorption, and mercury intrusion. Fuel 2013, 103, 606–616.

2. King HE; Eberle APR; Walters CC; Kliewer CE; Ertas D; Huynh C, Pore Architecture and Connectivity in Gas Shale. Energy & Fuels 2015, 29, (3), 1375–1390.

3. Bahadur J; Radlinski AP; Melnichenko YB; Mastalerz M; Schimmelrnannv A, Small-Angle and Ultrasmall-Angle Neutron Scattering (SANS/USANS) Study of New Albany Shale: A Treatise on Microporosity. Energy & Fuels 2015, 29, (2), 567–576.

4. Zhao JH; Jin ZJ; Hu QH; Jin ZK; Barber TJ; Zhang YX; Bleuel M, Integrating SANS and fluid-invasion methods to characterize pore structure of typical American shale oil reservoirs. Scientific Reports 2017, 7, 16. [PubMed: 28154412]

5. Rexer TF; Mathia EJ; Aplin AC; Thomas KM, High-Pressure Methane Adsorption and Characterization of Pores in Posidonia Shales and Isolated Kerogens. Energy & Fuels 2014, 28, (5), 2886–2901.

6. Pepper AS; Corvi PJ, SIMPLE KINETIC-MODELS OF PETROLEUM FORMATION .1. OIL AND GAS GENERATION FROM KEROGEN. Marine and Petroleum Geology 1995, 12, (3), 291–319.

7. Krevelen D. W. v., Coal: Typology - Physics - Chemistry - Constitution. Elsevier Scientific Pub. Co.: 1961.

8. Tissot BP; Welte DH, Petroleum formation and occurrence. Springer-Verlag Berlin Heidelberg: 1984.

9. Mccarthy K; Rojas K; Niemann M; Palmowski D; Peters K; Stankiewicz A, Basic petroleum geochemistry for source rock evaluation. Oilfield Review 2011, 23, (2), 32–34.

10. Magoon LB; Dow WG, THE PETROLEUM SYSTEM - FROM SOURCE TO TRAP. Aapg Bulletin-American Association of Petroleum Geologists 1991, 75, (3), 627–627.

11. Alexander T; Baihly J; Boyer C; Clark B; Waters G; Jochen V; Le Calvez J; Lewis R; Miller CK; Thaeler J; Toelle B;E, Gas shale revolution. Oilfield review 2011, 23, 40–55.

12. Passey QR; Bohacs K; Esch WL; Klimentidis R; Sinha S, From Oil-Prone Source Rock to Gas-Producing Shale Reservoir – Geologic and Petrophysical Characterization of Unconventional Shale-Gas Reservoirs. In International Oil and Gas Conference and Exhibition in China, Society of Petroleum Engineers: 2010.

13. Ambrose RJ; Hartman RC; Diaz-Campos M; Akkutlu IY; Sondergeld CH, Shale Gas-in-Place Calculations Part I: New Pore-Scale Considerations. Spe Journal 2012, 17, (1), 219–229.

14. Loucks RG; Reed RM; Ruppel SC; Jarvie DM, MORPHOLOGY, GENESIS, AND DISTRIBUTION OF NANOMETER-SCALE PORES IN SILICEOUS MUDSTONES OF THE MISSISSIPPIAN BARNETT SHALE. Journal of Sedimentary Research 2009, 79, (11–12), 848–861.

15. Milliken KL; Rudnicki M; Awwiller DN; Zhang TW, Organic matter-hosted pore system, Marcellus Formation (Devonian), Pennsylvania. Aapg Bulletin 2013, 97, (2), 177–200.

16. Loucks RG; Reed RM; Ruppel SC; Hammes U, Spectrum of pore types and networks in mudrocks and a descriptive classification for matrix-related mudrock pores. Aapg Bulletin 2012, 96, (6), 1071–1098.

17. Psarras P; Holmes R; Vishal V; Wilcox J, Methane and CO2 Adsorption Capacities of Kerogen in the Eagle Ford Shale from Molecular Simulation. Accounts of Chemical Research 2017, 50, (8), 1818–1828. [PubMed: 28762725]

18. Zhao HJ; Lai ZP; Firoozabadi A, Sorption Hysteresis of Light Hydrocarbons and Carbon Dioxide in Shale and Kerogen. Scientific Reports 2017, 7, 10. [PubMed: 28127059]

19. Gu X; Cole DR; Rother G; Mildner DFR; Brantley SL, Pores in Marcellus Shale: A Neutron Scattering and FIB-SEM Study. Energy & Fuels 2015, 29, (3), 1295–1308.

20. Hu H, Methane adsorption comparison of different thermal maturity kerogens in shale gas system. Chinese J. Geochemistry 2014, 33, (4).

21. Horvath Z. a. J., K.S. Procedure for the isolation of kerogen from sedimentary; Bureau of Mineral Resources, Geology and Geophysics: 1981.

22. Chiang WS; Georgi D; Yildirim T; Chen JH; Liu Y, A non-invasive method to directly quantify surface heterogeneity of porous materials. Nature Communications 2018, 9, 7.

23. Kline SR, Reduction and analysis of SANS and USANS data using IGOR Pro. Journal of Applied Crystallography 2006, 39, 895–900.

24. Lemmon E; Huber M; McLinden M, REFPROP, NIST Stand. Ref. Database 23, Version 9.0. In.

25. Zhou W; Wu H; Hartman MR; Yildirim T, Hydrogen and methane adsorption in metal-organic frameworks: A high-pressure volumetric study. Journal of Physical Chemistry C 2007, 111, (44), 16131–16137.

26. Turkoglu D; Chen-Mayer H; Paul R; Zeisler R, Assessment of PGAA capability for low-level measurements of H in Ti alloys. Analyst 2017, 142, (20), 3822–3829. [PubMed: 28952615]

27. Thomas JJ; Valenza JJ; Craddock PR; Bake KD; Pomerantz AE, The neutron scattering length density of kerogen and coal as determined by CH3OH/CD3OH exchange. Fuel 2014, 117, 801–808.

28. Wang Q; Liu Q; Wang ZC; Liu HP; Bai JR; Ye JB, Characterization of organic nitrogen and sulfur in the oil shale kerogens. Fuel Processing Technology 2017, 160, 170–177.

29. Sing KSW; Everett DH; Haul RAW; Moscou L; Pierotti RA; Rouquerol J; Siemieniewska T, Reporting Physisorption Data for Gas/Solid Systems. In Handbook of Heterogeneous Catalysis, Wiley-VCH Verlag GmbH & Co. KGaA: Weinheim, Germany, 2008.

30. Eberle APR; King HE; Ravikovitch PI; Walters CC; Rother G; Wesolowski DJ, Direct Measure of the Dense Methane Phase in Gas Shale Organic Porosity by Neutron Scattering. Energy & Fuels 2016, 30, (11), 9022–9027.

31. Pathak M; Kweon H; Deo M; Huang H, Kerogen Swelling and Confinement: Its implication on Fluid Thermodynamic Properties in Shales. Scientific Reports 2017, 7, 14. [PubMed: 28144039]

32. Bale HD; Schmidt PW, SMALL-ANGLE X-RAY-SCATTERING INVESTIGATION OF SUBMICROSCOPIC POROSITY WITH FRACTAL PROPERTIES. Physical Review Letters 1984, 53, (6), 596–599.

33. Wong PZ; Bray AJ, SMALL-ANGLE SCATTERING BY ROUGH AND FRACTAL SURFACES. Journal of Applied Crystallography 1988, 21, 786–794.

34. Gu X; Mildner DFR; Cole DR; Rother G; Slingerland R; Brantley SL, Quantification of Organic Porosity and Water Accessibility in Marcellus Shale Using Neutron Scattering. Energy & Fuels 2016, 30, (6), 4438–4449.

35. Mastalerz M; He LL; Melnichenko YB; Rupp JA, Porosity of Coal and Shale: Insights from Gas Adsorption and SANS/USANS Techniques. Energy & Fuels 2012, 26, (8), 5109–5120.

36. Debye P; Bueche AM, SCATTERING BY AN INHOMOGENEOUS SOLID. Journal of Applied Physics 1949, 20, (6), 518–525.

37. Debye P; Anderson HR; Brumberger H, SCATTERING BY AN INHOMOGENEOUS SOLID .2. THE CORRELATION FUNCTION AND ITS APPLICATION. Journal of Applied Physics 1957, 28, (6), 679–683.

38. Chiang WS; Fratini E; Baglioni P; Chen JH; Liu Y, Pore Size Effect on Methane Adsorption in Mesoporous Silica Materials Studied by Small-Angle Neutron Scattering. Langmuir 2016, 32, (35), 8849–8857. [PubMed: 27512895]

39. Chiang WS; Fratini E; Baglioni P; Georgi D; Chen JH; Liu Y, Methane Adsorption in Model Mesoporous Material, SBA-15, Studied by Small-Angle Neutron Scattering. Journal of Physical Chemistry C 2016, 120, (8), 4354–4363.

40. Chiang WS; Chen JH; Liu Y, Investigation of porous materials with large surface heterogeneity using the generalized Porod's scattering law method. Physical Review E 2019, 99, (4), 17.
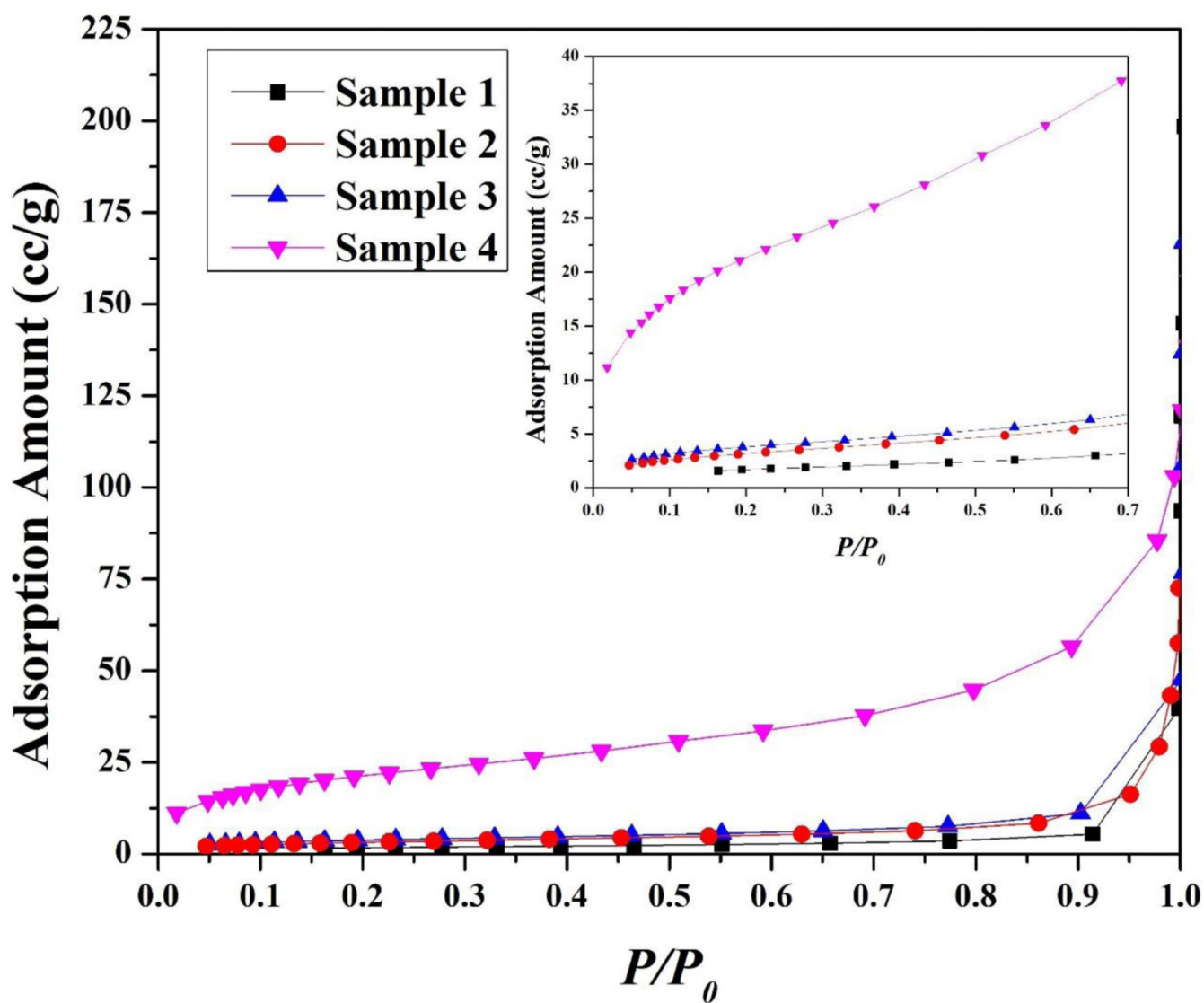
Figure 1.
Volumetric isotherm curves at 77 K for N_2 adsorption for four kerogens Sample 1, Sample 2, Sample 3, and Sample 4. The inset shows the enlargement of data at $P/P_0 < 0.7$.
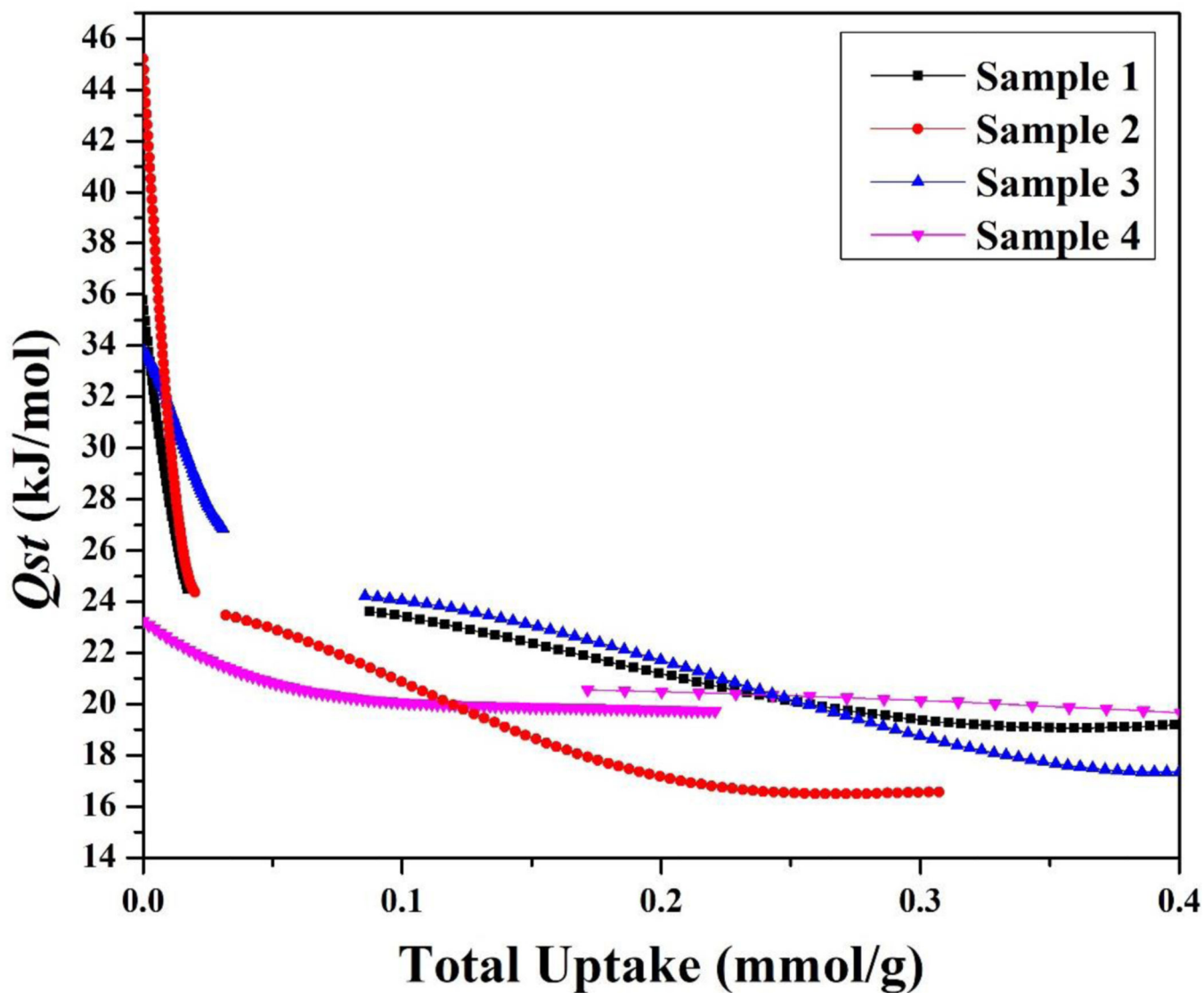
Figure 2.
Isosteric heat Q_{st} as a function of total uptake for the least mature kerogen, Sample 1, and the most mature kerogen, Sample 4.
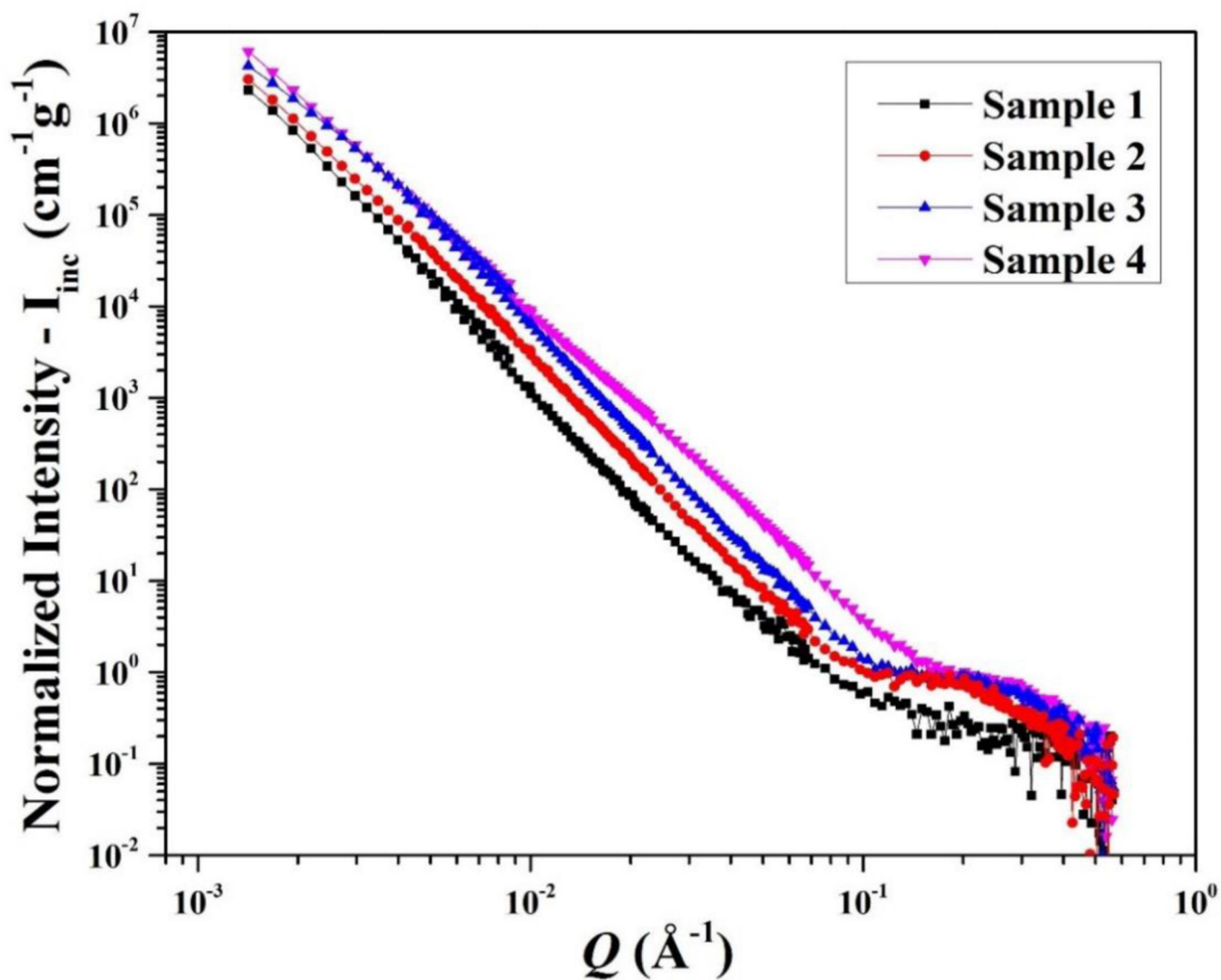
Figure 3.
Normalized SANS data by kerogen mass for four dry Sample 1, Sample 2, Sample 3, and
Sample 4. The samples were loaded in the Titanium cells with quartz windows, allowing
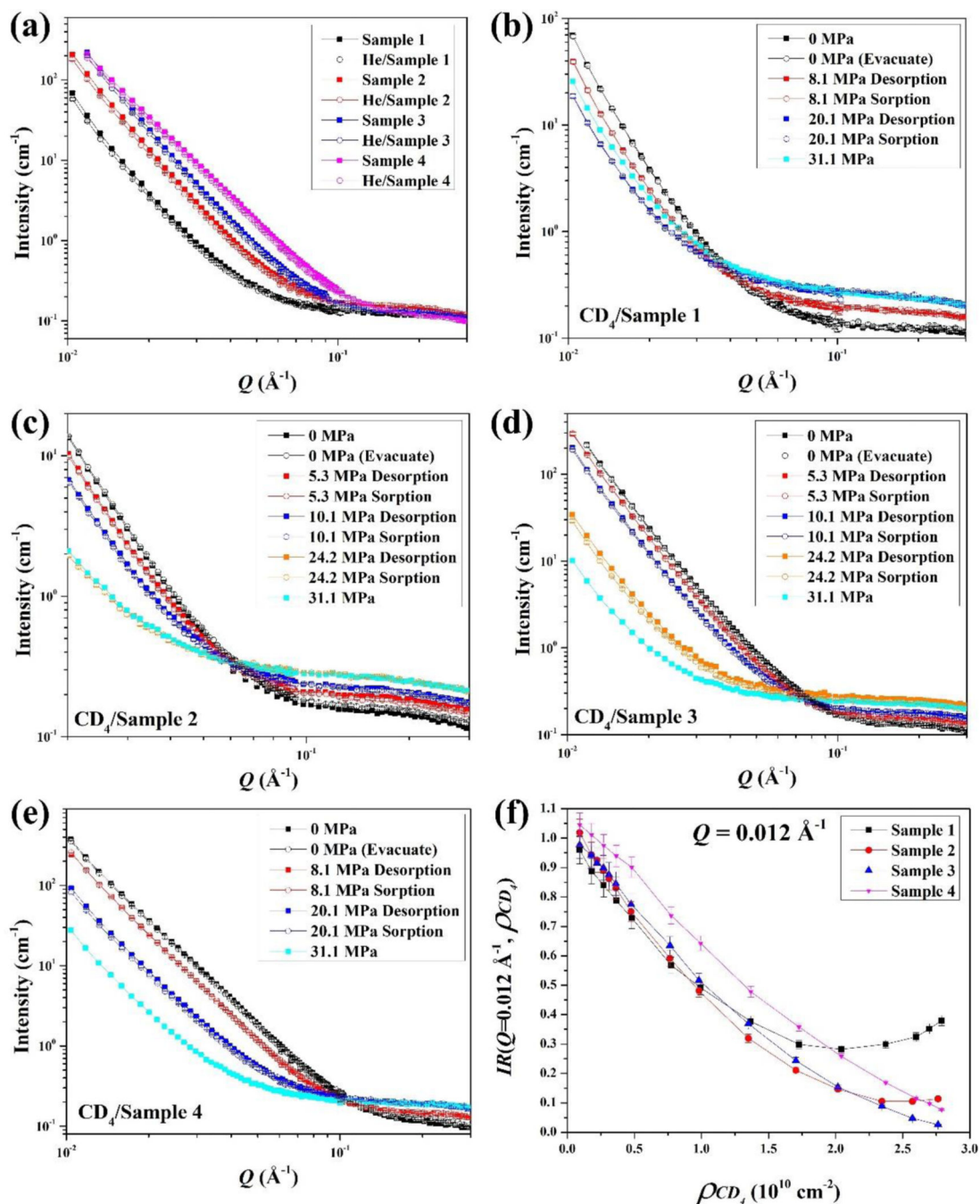SANS data to be measured at high Q region up to ~ 0.5 Å^{-1}.

Figure 4.
(a) SANS data of dry kerogens (solid squares) and kerogens loaded with 31.1 MPa helium (open circles); SANS data of kerogens during CD_4 desorption (solid squares) and adsorption (open circles) processes at different CD_4 pressures for (b) Sample 1, (c) Sample 2, (d) Sample 3, and (e) Sample 4. The SANS gas loading measurement procedure: (i) vacuum sample (0 MPa), (ii) loading 31.1 MPa CD_4, (iii) desorption, (iv) vacuum sample (0 MPa (Evacuate)), and (v) adsorption. (f) SANS intensity at $Q = 0.012$ Å^{-1} at CD_4 pressure with

bulk CD_4 scattering length density (SLD) = ρ_{CD4}, i.e. $I\left(Q = 0.012\mathring{A}^{-1}, \rho_{CD4}\right)$, normalized to $I\left(Q = 0.012\mathring{A}^{-1}, \rho_{CD4} = 0\right)$ as a function of ρ_{CD4} for the four kerogen samples.
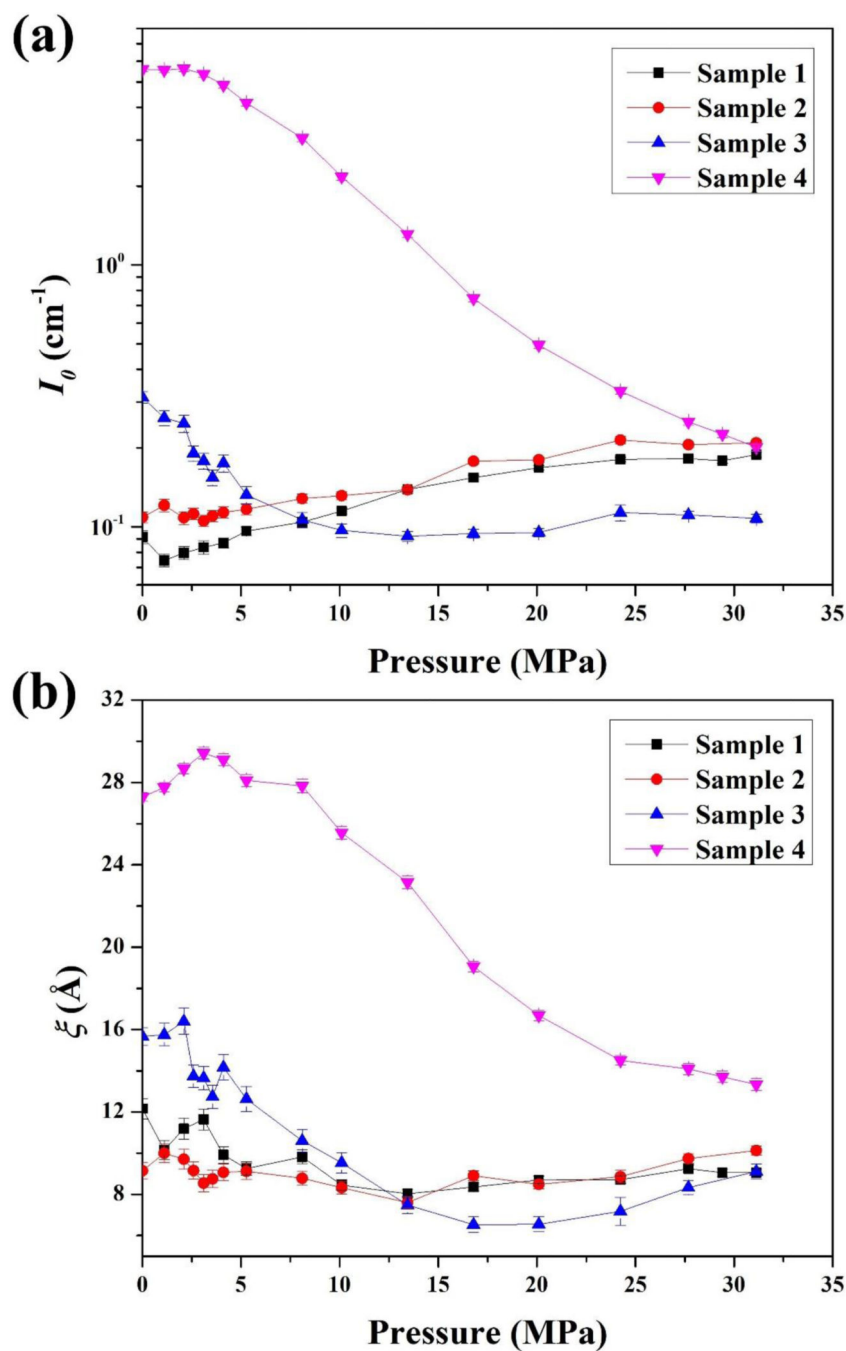
Figure 5.
Debye Anderson Brumberger (DAB) fitting results for (a) pre-factor I_0 and (b) correlation length ξ for four kerogens Sample 1 (least mature kerogen), Sample 2, Sample 3, and Sample 4 (most mature kerogen).
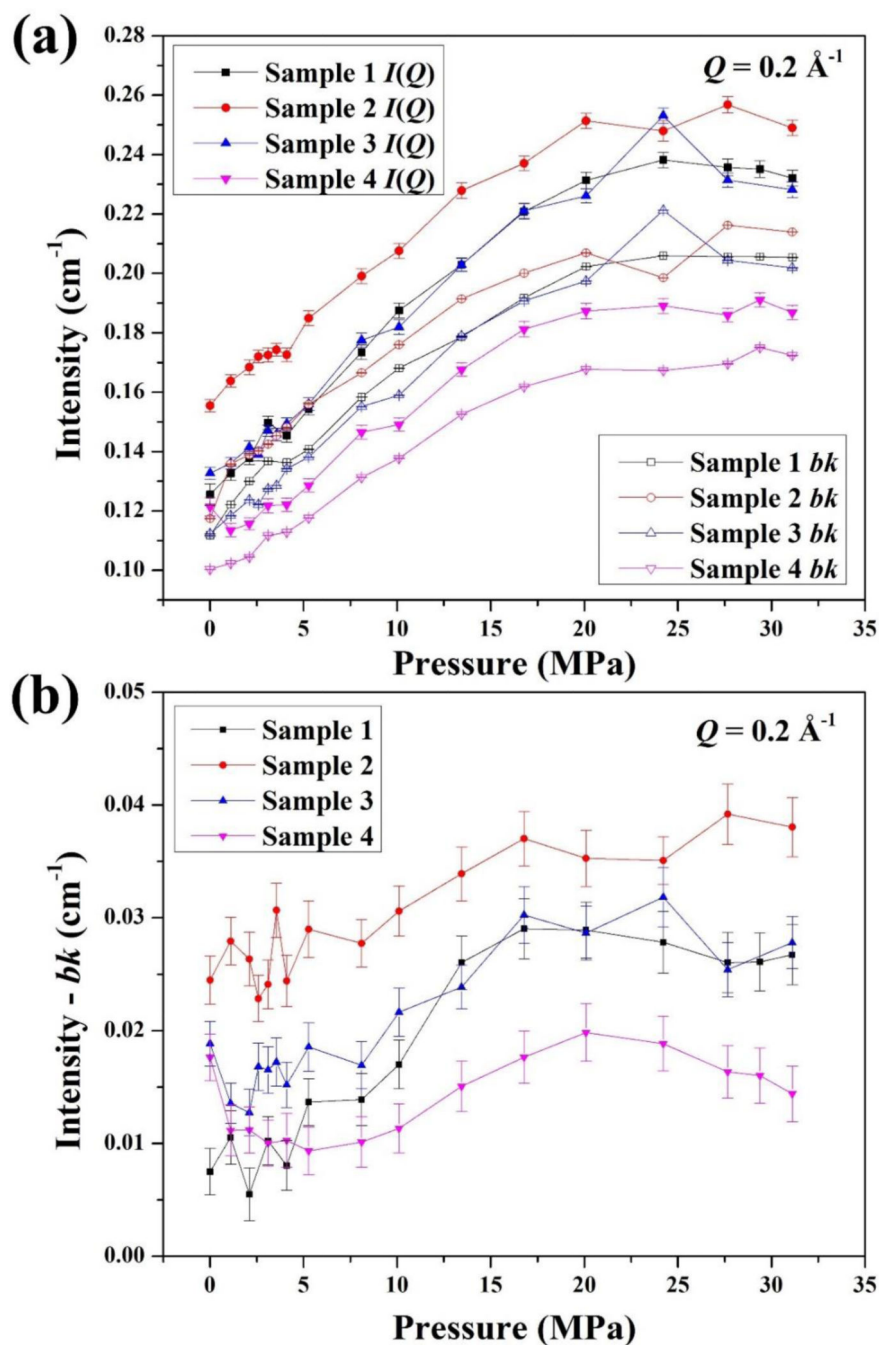
Figure 6.

(a) Absolute intensity at $Q = 0.2$ Å^{-1}, $I\left(Q = 0.2\,\text{Å}^{-1}\right)$, \ (solid symbols) together with the constant backgrounds, bk, (open symbols) found by the slope of the plot $I(Q) * Q^4 v_s . Q^4$ using the data between 0.1 Å^{-1} to 0.3 Å^{-1} and (b) intensity after subtracting bk, $I\left(Q = 0.2\,\text{Å}^{-1}\right) - bk$, of gas loading kerogens at different pressures.

Table 1.

Atomic ratio relative to carbon obtained from PGAA

Sample ID	R_0 (%)	H/C	Fe/C	S/C	N/C	2*Fe/C
Sample 1	0.62	1.02 ± 0.04	0.058 ± 0.003	0.113 ± 0.006	0.025 ± 0.003	0.116 ± 0.006
Sample 2	1.02	0.93 ± 0.04	0.100 ± 0.005	0.196 ± 0.009	0.018 ± 0.002	0.20 ± 0.01
Sample 3	1.59	0.63 ± 0.03	0.057 ± 0.003	0.110 ± 0.005	0.015 ± 0.002	0.114 ± 0.006
Sample 4	2.26	0.42 ± 0.02	0.0149 ± 0.0006	0.027 ± 0.001	0.016 ± 0.002	0.030 ± 0.001

Table 2.

Properties of Kerogens

Samples	Vitrinite Reflectance (%)	BET Surface Area^a (m²/g)	Pore Volume^{a,b} (cc/g)	Methane Isosteric Heat $Q_{st,0}$^{c} (kJ/mol)
Sample 1	0.62	5.94	0.06	35
Sample 2	1.02	11.79	0.07	44
Sample 3	1.59	13.77	0.07	33.6
Sample 4	2.26	78.03	0.16	23

^{a}Obtained from N_2 volumetric adsorption isotherm measurements at 77 K.

^{b}Using $P/P_0 = 0.98$ to calculate the pore volume.

^{c}Obtained from N_2 volumetric adsorption isotherm measurements at 273 K and 296 K, see SI for more details.

Table 3.

Parameters Extracted from Generalized Porod's Scattering Law Method (GPSLM)[a]

Sample ID	R_0 (%)	ρ_A (×10^{-6}Å^{-2})	$\rho_M{}^2$	Δ_H [b]	S_{GPSLM}
Sample 1	0.62	2.10 ± 0.02	6.2 ± 0.2	0.29 ± 0.02	3.8 ± 0.1
Sample 2	1.02	2.80 ± 0.06	8.5 ± 0.3	0.09 ± 0.05	7.3 ± 0.3
Sample 3	1.59	3.6 ± 0.1	12.5 ± 0.7	~ 0	10.6 ± 0.6
Sample 4[c]	2.26	5.9 ± 0.6	27 ± 3	~ 0	N/A

[a] ρ_A and Δ_H are obtained from fitting Figure 4(f) with eq 2. $\rho_{2M}{}^2$ and S_{GPSLM} are determined by $\rho_{2M}{}^2 = \dfrac{\rho_A{}^2}{1 - \Delta_H{}^2}$ and eq 8, respectively.

[b] Δ_H should be a positive value. However, for Sample 3 and Sample 4, Δ_H is very close to 0 and the fitting values become negative. Therefore, we assign Δ_H to 0 manually for these two samples.

[c] The extended GPSLM is applied to Sample 4 because the sample has a fractal surface.